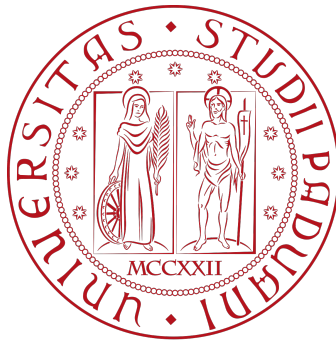# UNIVERSITÀ DEGLI STUDI DI PADOVA

DIPARTIMENTO DI FISICA E ASTRONOMIA "Galileo Galilei"

CORSO DI LAUREA IN FISICA

Study of an alternative extraction electrode for particle accelerator of NIO1 experiment

Laureando:
ANDREA LUDOVICI

Relatore: Dott. GIANLUIGI SERIANNI
Correlatore: Dott. PIERLUIGI VELTRI

ANNO ACCADEMICO 2016/2017

Abstract

The NIO1 experiment is a compact and modular negative ion source built at Consorzio RFX, Padua, with the aim to investigate the optimal configuration for a negative ion source of the type needed for the nuclear fusion experiment ITER. Negative ions, produced in a cold plasma, are extracted from it by an intense electric field, generated by applying a potential of some kilovolts to an electrode called "extraction grid" (EG). This electrode has permanent magnets in it, needed to deflect the electrons that are unavoidably extracted from the source. A new EG, completely redesigned with respect to the original one has been recently installed on NIO1. The aim of this thesis consists in following the installation of such electrode, contributing to the preliminary measurements of the embedded magnets. To evaluate the impact of the new electrode on the optics of the negative ion beam a set of numerical simulations were carried out. The calculations were performed using a numerical model developed ad hoc during the thesis. The model is based on the IBSimu environment, a tool commonly used to model accelerators in high energy physics. As part of my work I adapted IBSimu to describe for the first time an accelerator used in nuclear fusion field. The model was validated against similar codes, and finally used to interpret the experimental measurements performed in the NIO1 accelerator.

Table of Contents

1 Introduction

1.1 Thermonuclear fusion

The production of energy from nuclear fusion [1] could represent a clean way to supply the global increasing energy demand and differs from other form of innovative energy generation in terms of fuel availability, environmental protection, safety and weather self-sufficiency (unlike wind and solar power).

Nuclear fusion is a reaction in which two or more light nuclei collide and fuse producing one or more nuclei. The difference in mass between the products and reactants is manifested as kinetic energy of the products. For such a reaction to occur, the colliding nuclei need to have enough kinetic energy to overcome Coulomb repulsion. If the matter is sufficiently heated (temperatures in order of $10^7 - 10^8$ K), hence being plasma, the fusion reaction may occur due to collisions with extreme thermal kinetic energies of the particles.

The most advantageous reactions for a nuclear fusion reactor are with deuterium (D) and tritium (T) due to the high cross section at low temperature as in table 1.1.

$$D + D \rightarrow {}^3He + n \tag{1.1}$$

$$D + D \rightarrow T + p \tag{1.2}$$

$$D + T \rightarrow {}^4He + n \tag{1.3}$$

The two branches 1.1 and 1.2 occur with an approximately equal likelihood. Data on these reaction are given in table 1.1 [2].

Table 1.1: Fusion reactions: cross sections at centre-of-mass energy of 10 keV and 100 keV, maximum cross-section σ_{max} and location of the maximum ϵ_{max}.

Reaction	σ (10 keV) [barn]	σ (100 keV) [barn]	σ_{max} [barn]	ϵ_{max} [keV]
$D + T \rightarrow {}^4He + n$	2.72×10^{-2}	3.43	5.0	64
$D + D \rightarrow T + p$	2.81×10^{-4}	3.3×10^{-2}	0.096	1250
$D + D \rightarrow {}^3He + n$	2.78×10^{-4}	3.7×10^{-2}	0.11	1750

1.2 ITER project

ITER will be the largest experiment on thermonuclear fusion obtained with a magnetically confined plasma that has been designed to prove the feasibility of fusion as a large-scale and carbon-free source of energy [3]. The project was first launched in 1985 and it is now being built in southern France by a collaboration of 35 nations.
The aim is to obtain an energy factor, i. e. the ratio between the power produced with respect to the external power supplying the reactor, of about 10.
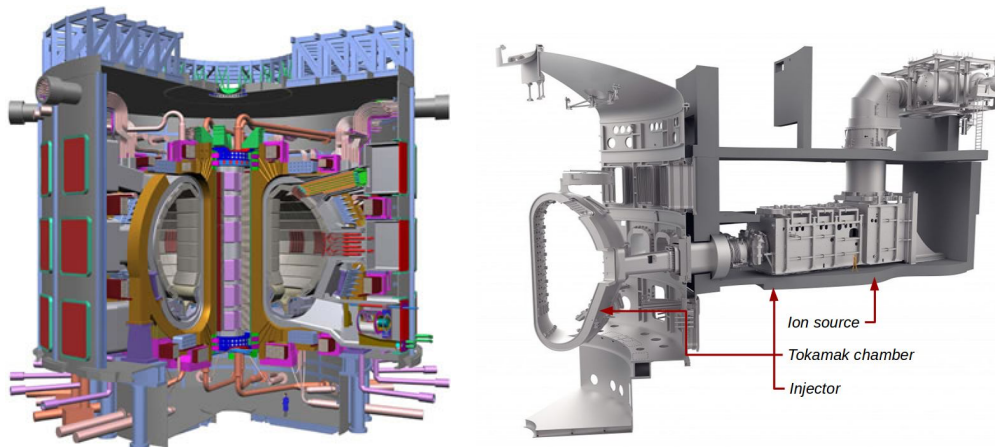

Figure 1.1: Left: Model of ITER machine [4]. Right: ITER neutral beam system.

In order to get the high temperature ($\sim$ 10keV) needed for fusion reaction, ITER includes external heating systems. The additional heating systems are radio frequency heating, in which high frequency electromagnetic waves are used, and neutral beam injection.

Two neutral beam injectors (figure 1.1), each one delivering a deuterium beam of 16.5 MW with particle energies of 1 MeV, are currently foreseen for ITER. A third neutral beam will be used for diagnostic purposes.

1.3 Neutral beam injectors

Neutral beam injection heating consists in shooting high energy neutral particles into the plasma. The high-energy particles used to heat the plasma have to be neutral in order to overcome the strong magnetic field used to confine plasma. Here high energy deuterium atoms up to an equivalent current of 40 A and energy of 1 MeV are used. Once the neutral particle is inside the plasma, it gets rapidly ionized through collisions and the confined by the magnetic field. Since particle kinetic energy is large compared to plasma temperature, they deliver energy to the plasma by collisions.

A neutral particles beam can only be created indirectly: since neutral particles are not subject to electromagnetic fields, in order to make them reach the required energy to heat plasma, they are generated as ions. Then they can be accelerated as an ion beam by means of strong electric fields between different grids of an electrostatic accelerator. The next step is neutralization in stripping processes for negative ions or charge exchange processes for positive ions with a neutral gas stripper. Ions which did not get neutralized are filtered by a strong electrostatic field inside the residual ion dump (RID).

The ions created in the source can be either positive or negative. Even if the majority of existing neutral beam injector exploits the acceleration of positive ions, in order to get a highly energetic beam, negative ions are needed. The ionizing cross section of a beam decreases with the beam energy, hence, in order to allow the beam to reach the plasma core, which is almost after 2 meters of plasma for ITER, without being completely ionized before, a high beam energy is required. At these energies neutralization efficiency for positive ions is much less than negative ions as shown in figure 1.2 therefore a negative source has been chosen for ITER.
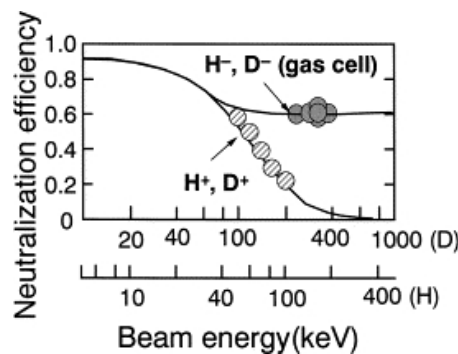

Figure 1.2: Neutralization efficiency for positive and negative deuterium and hydrogen ions as a function of the particle energy.

1.3.1 Negative ion sources

The negative ions are generated inside an ion source. The simplest ion source features a plasma chamber to confine the plasma, a gas feed line and an electrostatic extractor to let the ions out.

Plasma into ion sources can be generated in two different ways. The first source type is composed of an hot cathode (i. e. tungsten filament), which emits electrons by thermionic effect. Tungsten filaments have to be replaced periodically and filament evaporation produces impurities. For ITER a Radio Frequency source has been chosen: a coil wound around the source wall is used to generate an inductive discharge. Due to the high-frequency electromagnetic waves emitted by the coil, acting as an antenna, the free electrons in the source gain enough energy to ionize the background gas forming a

plasma. In a RF discharge, if the imposed frequency is lower than the electron plasma frequency f, given by 1.4, then the electrons can follow the oscillation producing ionising collision and, hence, a plasma.

$$f = \frac{1}{2\pi}\sqrt{\frac{ne^2}{\epsilon_0 m}} \tag{1.4}$$

where n is the electron density and m is the mass of the electron. ITER source works with a frequency of 1 MHz.
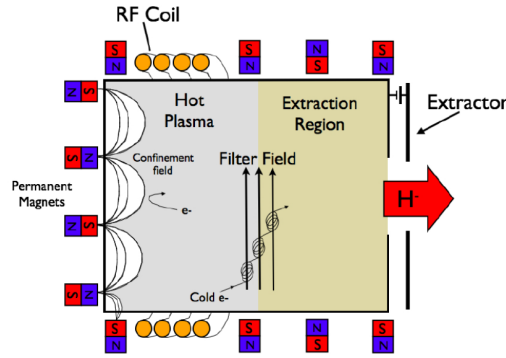

Figure 1.3: Schematic of a RF driven negative ion source, with magnetic filter and electrostatic extractor.

A negative ion is formed when an atom or a molecule captures an electron into an electron affinity level. There are two different physical mechanisms responsible for this: volume production, if the atom or molecule captures a free electron of the plasma itself, and surface production, in which the electron is shifted from the conduction band of a metal surfaces surrounding the plasma [5]. The efficiency of the latter process can be enhanced if the work function of the surface is lowered by depositing on it a material with a low work function[6] [7]. Cesium is the element with the lowest work function [8]. With no cesium coverage the metal surface has its intrinsic work function but as cesium is deposited the work function decreases with increasing coverage reaching a minimum for a value of about 0.6 monolayers.

Volume production needs two step processes [9]: vibrational excitation and dissociative attachment wit electrons. If a neutral molecule, like H_2, is in a vibrational state (v) it can capture the electron. The resulting H_2^- is unstable (with a lifetime of about 10^{-14} seconds) and dissociate in $H^0 + H^-$. Therefore at first a neutral molecule has to be vibrationally excited by collision with an electron

$$e^- + H_2 \rightarrow e^- + H_2(v >> 0) \tag{1.5}$$
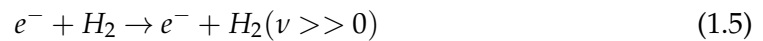
then negative hydrogen ions can be created by dissociative attachment involving a low energy electron and the excited molecule.

$$e^- + H_2(v >> 0) \rightarrow H_2^- \rightarrow H + H^- \tag{1.6}$$
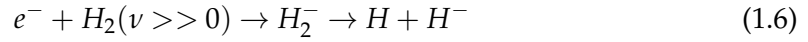
The first process is more likely with high incident electron energies $E_e > 20eV$ and the second process need energies of less than 1eV. This is why two populations of electrons with different temperatures are required.

The source has to be divided in two parts, a hotter upstream region called "driver", where the electrons produce vibrationally excited molecules, and a cooler downstream region called "extraction region", where negative ions are produced and extracted. A magnetic filter between the two regions allows to reduce the temperature of electrons diffusing from the driver to the extraction region. The magnetic filter is based on the dependence of the electron transversal diffusivity across a magnetic field $D_\perp$ on the -1/2 power of the electron temperature T.

$$D_\perp \propto \frac{1}{\sqrt{T}} \tag{1.7}$$

1.3.2 Accelerators

The simplest type of extraction system is the diode type consisting in two separate electrodes as in figure 1.4, ITER extraction system is an upgrade made of seven electrodes. In this simple type of systems three steps in acceleration can be distinguished: electrostatic extraction of the ions from the source, pre-acceleration (typically to 100keV) and full energy acceleration (1MeV is considered for ITER)[5].
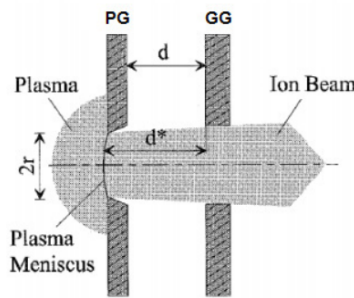

Figure 1.4: Diode type acceleration system.

The electrode facing the plasma is the extraction electrode which is negatively biased with respect to the other electrode. The potential difference between the two electrodes is responsible for extraction and acceleration of the ions.

The boundary region between the plasma in the source and the vacuum of the accelerator is called meniscus which is usually identified as the zero potential surface. Meniscus shape mainly depends on electrode voltage and plasma density and it should be a convex lens which determines the initial beam quality.

The maximum extractable ion current density is determined by the balance between the electrical potential applied to the electrodes and the space charge of the negative charges between the electrodes: the maximum extractable current density can not grow with no limit but saturates since the negative charges accumulated in the extraction region screen the electric field. This can be mathematically expressed by the Child-Langmuir equation [10] which is the solution of Poisson equation in the case of a planar and infinite emission area (see eq. 1.8)

$$j_{max} = \frac{4}{9}\epsilon_0 \sqrt{\frac{2eZ}{m}} \frac{1}{d^2} V^{\frac{3}{2}} \tag{1.8}$$

where ϵ_0 is vacuum permittivity, Z is the ion charge state, m the ion mass, d the gap between the electrodes, V the potential drop and e the absolute value of the electron charge. Considering a cylindrically-symmetric extraction system with an extraction electrode hole radius r, the total ion beam current is given by

$$I_{max} = \frac{4}{9}\pi\epsilon_0 \sqrt{\frac{2eZ}{m}} \left(\frac{r}{d}\right)^2 V^{\frac{3}{2}} \tag{1.9}$$

then the ion current is proportional to $V^{\frac{3}{2}}$ by a proportionality constant called perveance P.

A simple scaling law can be derived at fixed geometry: holding perveance constant at different values V and V' of voltage and different values I and I' of current.
From

$$I_{max} = PV^{\frac{3}{2}} \tag{1.10}$$

we get

$$V' = \left(\frac{I'}{I}\right)^{\frac{2}{3}} V \tag{1.11}$$

therefore if the current is scaled by a factor η, scaling the voltage by a factor $\eta^{\frac{2}{3}}$ does not change the optics.

A way to characterize the optics of a particle beam is given by the definition of divergence δ. For a cylindrically-symmetric beam we can define δ as an angular measure of the increase in beam diameter or radius with distance from where beam emerges.

The optimum perveance condition is reached when the divergence is at its minimum value: with increasing P, the divergence decreases (this region is called under-perveant

region) reaching its minimum, then it increases again (over-perveant region).

Beam quality also depends on plasma electrode shape as shown in figure 1.5. If the inner face of the source plasma electrode is nearly flat (a), H^- are emitted towards the plasma and it is difficult for them to reach the extraction. With a flat plasma electrode exit even if rays start parallel, outer rays are repelled by inner ray space charge so beam enlarges (b). With a conical face, the acceleration force has an inward focusing component making a parallel ray equilibrium possible (c). It can be shown that the best condition is reached with and angle called Pierce angle of $\frac{3\pi}{8}$.
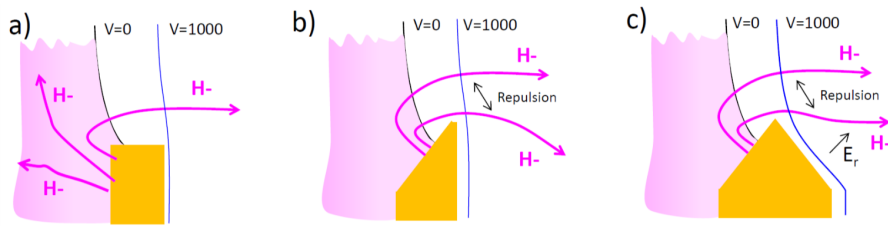

Figure 1.5: Beam quality dependence on plasma electrode shape.

Since, in negative beam accelerators, electrons are extracted together with ions, transversal magnetic fields generated from magnets put in the electrode are used to deflect electrons before they gain too much energy. In a magnetic field ions are deflected too but deflection is smaller to the one of electrons since their ratio is proportional to $\sqrt{\frac{m_e}{m_i}}$.

High current accelerators usually do not have only one aperture on the electrodes: there is the need for a multi aperture system. Since the aspect ratio (i. e. $\frac{r}{d}$) must be less than 0.5 to have a good divergence [11], many apertures are needed in order to achieve high current.

1.4 NIO experiment

The negative ion source NIO (Negative Ion Optimization) is a test facility which came into operation in 2014 at Consorzio RFX in Padua (IT) [12]. Its main purpose is to investigate the optimal conditions for a negative source like the one needed for ITER. Unlike ITER injectors, NIO is characterised by a high modularity (see figure 1.6) which allows rapid changes in the experimental setup. NIO's source can work with various gasses: at present hydrogen is being used.
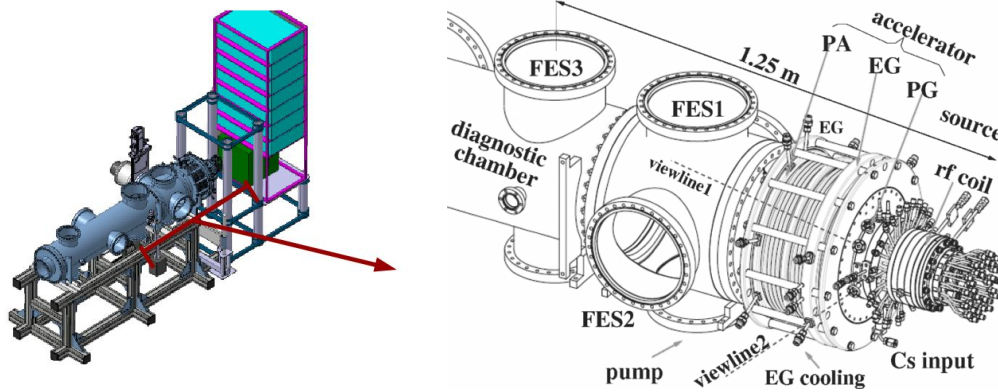
Figure 1.6: NIO design. FES1, FES2 and FES3 are possible positions for fast emittance scanners.

NIO structure can be divided in three main parts: the plasma source, negative ion extraction and acceleration region and beam diagnostic tube [13] (see figure 1.6).

The plasma source is a 70 millimeters long cylindric chamber with a 100 millimeters internal radius [14]. A 7-turn coil is wound around the chamber in order to create plasma by inductive coupling (with RF coupling frequency of $2 \pm 0.2 MHz$).

The accelerating column consists of four copper grids, equally spaced by 14 millimeters, with a 3x3 matrix of 3.8 mm radius apertures:

- Plasma Grid (PG), is the grid facing the plasma and is held at $-60kV$, which is approximately the same potential of the source.

- Extraction Grid (EG), is held at higher potential than the PG ($-52kV$).

- Post Acceleration grid (PA), held at ground potential.

- Repeller grid (REP), which can be slightly positively biased (up to $150V$) to suppress backstreaming of positive ions.

All the grids are water cooled and the extraction grid is insulated from the post acceleration grid by two insulating ceramic rings made of allumina. Another ring insulates EG from PG. Nominal values are $15mA$ current for each beamlet providing an ion current density of $300A/m^2$.

Finally the diagnostic chamber is constituted by metallic tube in which several holes allow diagnostics to be placed for the study of beam parameters.

2 NIO Extraction Electrode Optimization

The design of a new ion extraction system for NIO facility was started in order to optimize the beam optics with alternative electrostatic and magnetic configurations. The accelerator has been modified by completely replacing the extraction grid: the new electrode will feature new slots between the apertures, to place additional magnets, useful to optimize the electron filtering and residual ion deflection.

2.1 Ion extraction region

Negative ions are extracted from 9 apertures (in a 3x3 pattern) with a total extraction area of $400mm^2$ by a three electrode system. The first electrode, directly facing the plasma, is called Plasma Grid (PG) the second and third one are Extraction Grid (EG) and Post Acceleration Grid (AG) which extract and accelerate ions respectively (see figure 2.1). Repeller (REP) prevents drain of positive ions.
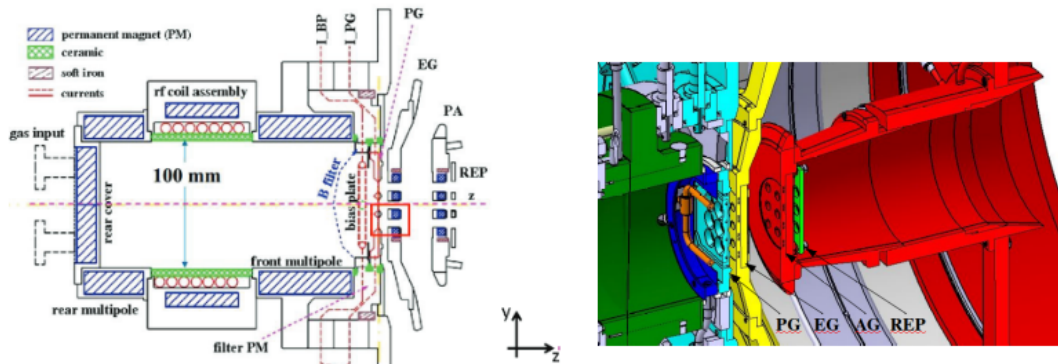

Figure 2.1: Schematic view of NIO.

These electrodes are realized by electro-deposition of copper and successive milling and include empty channels for water cooling and slots for magnets.

In the EG four array of CESM (Co-extracted Electrons Suppression) magnets are embedded to prevent the acceleration of co-extracted electrons, with magnetization along the acceleration direction z (see figure 2.1). CESM produces a magnetic field having the component B_x negligible compared to B_y and B_z at beamlet position. Since beam velocity along z axis is greater than the velocity along x and y axis, beam deflection is mainly due to B_y component and it is in x direction. Each column of beamlets is deflected in
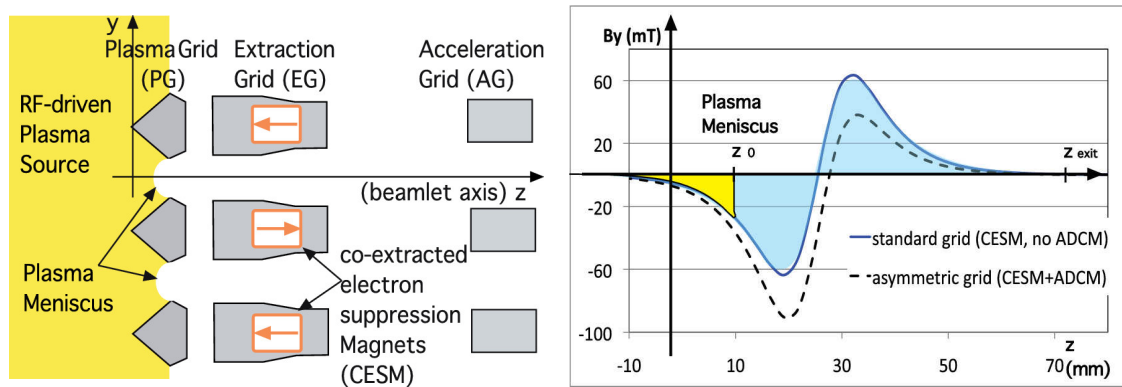
9

opposite directions (see figure 2.2).

Figure 2.2: Left: cross-section of PG, EG and AG[15]. Right: profiles of transverse magnetic field B_y along a beamlet axis[15].

A typical profile of the B_y component of magnetic field for a line passing on the beamlet axis from CESM configuration is shown in figure 2.2 (right figure, blue line) and it exhibits a symmetric double-swing profile.

Magnets are set also in the PA in order to support the disposal of stripped electrons and partially recover the primary beam alignment after the deflection induced by the EG magnets. In fact magnetic field from magnets in EG has to be compensated by opposite fields in order to remove any deflection of the H^- beam: one must ensure

$$\int_{z_0}^{z_{exit}} B_y \, dz = 0 \tag{2.1}$$

along the beam path since the deflection δ can be estimated, according to "paraxial approximation" formula as (see [15])

$$\delta = \frac{v_{x,exit}}{v_{z,exit}} = \frac{q \int_{z_0}^{z_{exit}} B_y \, dz}{m v_{z,exit}} = \sqrt{\frac{q}{m}} \frac{\int_{z_0}^{z_{exit}} B_y \, dz}{\sqrt{2 U_{exit}}} \tag{2.2}$$

where q and m are the ion charge and mass, U_{exit} is the electrostatic acceleration potential and z_0, z_{exit} are the initial and final axial coordinates of the ion trajectories.

2.1.1 Cancellation of the ion deflection

The negative ions are formed mainly at the border of the plasma source region and magnetic deflection of the ion beamlets is taken into account from plasma meniscus (border of yellow area at position z_0 in left figure 2.2) [15]. That is why integral 2.1 is computed from z_0. This assumption is based on the physical fact that ions and electrons are highly collisional and move diffusively in the plasma volume until they are accelerated by the

extraction electric field in the extraction volume where they are less collisional and suffer from the deflection induced by the B field.

For this reason, even if the magnetic field profile is perfectly symmetric along the beam axis, its effect on beam particle is not, because ion do not feel the tail of the B profile bulging inside the plasma. Nonetheless, an asymmetric configuration to compensate this effect can be produced by an additional arrangement of permanent magnets embedded in EG and such asymmetry can be calibrated so that the resulting deflection of the ions is cancelled. This calibration can be done either varying the thickness of the magnets along the direction x or by using materials having different magnetic remanence. These magnets are alternatively magnetized along the vertical direction and are called Asymmetric Deflection Compensation Magnets (ADCM) because they enhance the vertical component B_y on the upstream side of the EG and reduce it on the downstream side. Thus the B_y profile become asymmetric as shown in figure 2.2 (right figure, black dashed line).

Figure 2.3 shows the CESM and ADCM+CESM configurations studied for the new EG [16].
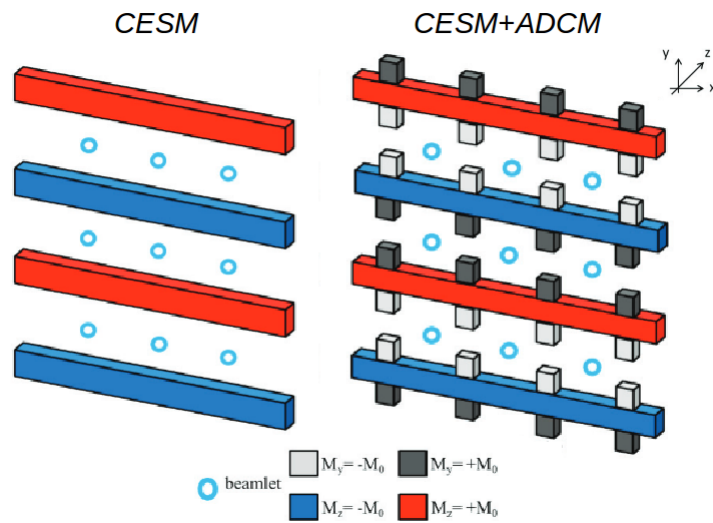

Figure 2.3: EG magnets configurations.

ADCM combines the features of a standard CESM with those of a planar Halbach array [15]. In 1980 Halbach showed that permanent magnet bars arranged around a cylindrical cavity can produce a dipole (or multipole) magnetic field inside the cavity and negligible field outside [17]. This concept has been applied to planar structures called Halbach arrays as shown in figure 2.4.
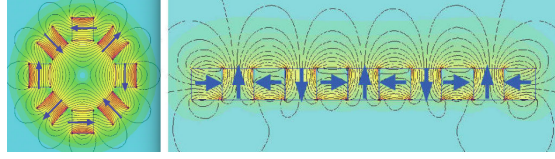
Figure 2.4: Maps of quadrupole magnetic field produced by permanent magnet bars arranged around a cylindrical cavity and planar Halbach array[15].

Two positive consequences follow from this new configuration of magnets: the increase in co-extracted electrons suppression thanks to the concentration of the magnetic field on the upstream side of the grid and, consequently, the possibility to reduce the size of CESM. This is beneficial to the design of the EG [18].

It has to be marked that the unconditional increase of B_y upstream peak can have some drawback: if electrons are deflected too much, they can spin around the extraction gap and this will increase the breakdown probability between PG and EG.

2.2 Design of the new extraction grid

The first set of NIO grids described in the previous section has been installed and tested [19]. The modification of the extraction grid is based on theoretical advantage of enlarging the EG apertures with an increase chamfer at the hole exit [18] and studies on ADCM configurations [16] as discussed in subsection 2.1.1. See figure 2.5 for a comparison between new EG and old EG layout [16].
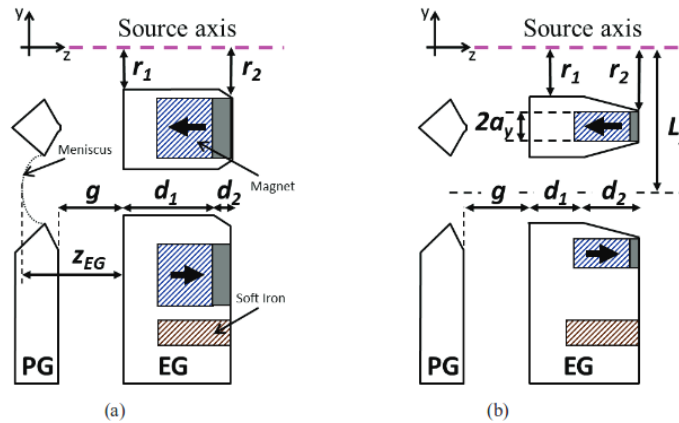

Figure 2.5: Top view on (a) old EG layout and (b) new EG layout.

With reference to the EG apertures the entrance radius r_1 has been increased from 3.2 to 3.5 mm, the exit radius r_2 from 4.1 to 5 mm, keeping the same grid thickness $d_1 + d_2 = 10.3mm$. Dimension d_1 has been decreased from 8.8 mm to 4.8 mm and the gap distance g between PG and EG can be adjusted in the range $g = 5 \pm 1mm$. As a consequence, the electric field penetrate deeply enhancing the convergence effect of the electrode.

Concerning the magnetic configuration, the old EG array CESM (with 4 vertical arrays of dimensions $5.2mm \times 5.8mm \times 64mm$) feature SmCo magnets with $B_r = 1.02T$ which proved to generate a B_y component too strong for an Hydrogen beam, thus a reduced B_r or size is needed: this has been done replacing SmCo magnets with a set of Ferrite ones.

The design criteria to fulfill are zero residual ions deflection after PA and complete electron deflection on the EG surface. The design procedure has been carried out checking the results of theoretical considerations and simulations performed by numerical tools over various sets of magnets.

2.3 Measurements of magnetic field

Before substituting the old EG with the new one having the new magnetic configuration, measurements of the magnetic field y component along z axis have been done in order to compare experimental results with simulations done using Opera electromagnetic finite element analysis simulation software [20]. Magnetic measurements have been made using a F.W.Bell Model 6010 Gauss/Tesla meter [21] with a transverse Hall probe like the one shown in figure 2.6 which allows to measure magnetic field component perpendicular to its largest surface.

A current is passed through the conductor which, when placed in a magnetic field, has a "Hall effect" voltage developed across it. When a conductor is placed in a magnetic field perpendicular to the direction of the electrons, they will be deflected from a straight path. As a consequence, one plane of the conductor will become negatively charged and the opposite side will become positively charged. When the force on the charged particles from the electric field balances the force produced by magnetic field, the separation of them will stop. If the current is not changing, then the Hall voltage is a measure of the magnetic flux density.
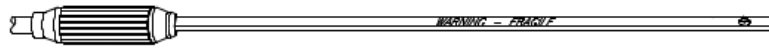

Figure 2.6: Transverse Hall probe.

A preliminary remanence measurement of single magnets has allowed to choose the set of magnets better satisfying required conditions of remanence uniformity at a fixed distance. In order to make magnetic measurement of the overall magnet configuration, single magnets were assembled in an extraction grid mock-up. A picture of mock-up with some magnets, is shown in figure 2.7(a) and figure 2.7(b) for the fully assembled mock-up.
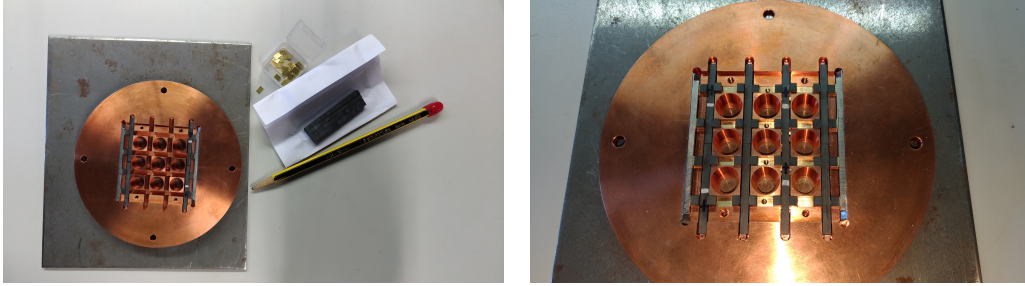
Figure 2.7: (a) Left: prototype during assembly. (b) Right: assembled prototype.
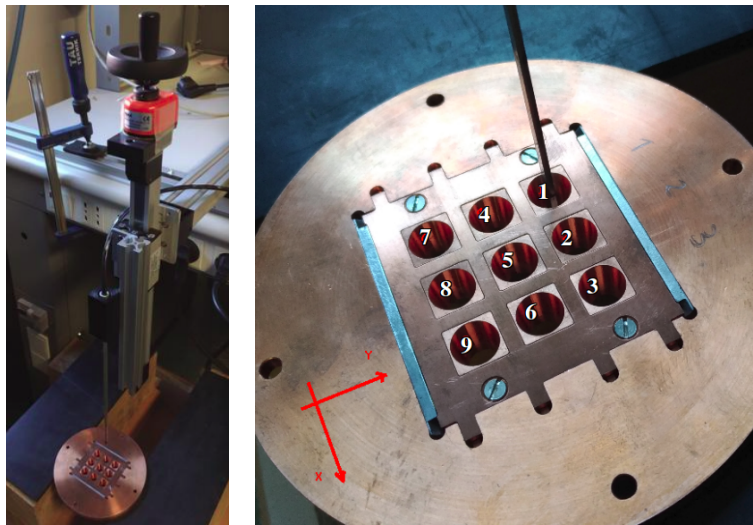

Figure 2.8: (a) Left: Actuator and probe system. (b) Right: Prototype with system of reference and beamlet enumeration.

The probe zero value was set while having the probe itself in a zero flux chamber in order to have a shield from external magnetic fields. Measurements were made every $1mm$ for a range of about $90mm$ along z axis. Position along z direction could be detected by using a 3-axial manual actuator as in figure 2.8. This procedure was repeated for every aperture of the grid. Central position along x and y direction was find as the x and y coordinates where B_y assumed the maximum value.

Results of measurements are shown in figure 2.9, 2.10 and 2.11 together with Opera simulations for three beamlets (1, 5, 9). See figure 2.8 for beamlet enumeration. Measurements are in a good agreement with simulations and profile of transverse magnetic field B_y is asymmetric as expected (see figure 2.2). The remaining beamlets are in agreement with simulations too and are not shown for brevity.

Opposite polarization of magnetic field for adjacent columns can be deduced from figures 2.9 and 2.10: beamlets 2, 5, 8 perceive an opposite in direction B_y respect to the

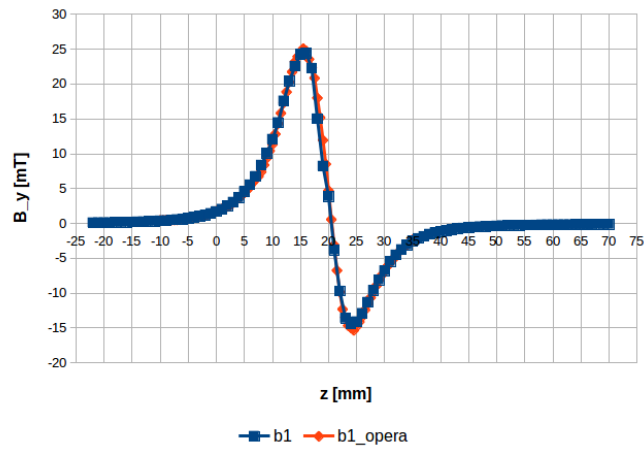one perceived by beamlets 1, 4, 7 and beamlets 3, 6, 9.

Figure 2.9: Plot of measurements (blue) and Opera simulations (orange) for beamlet 1.
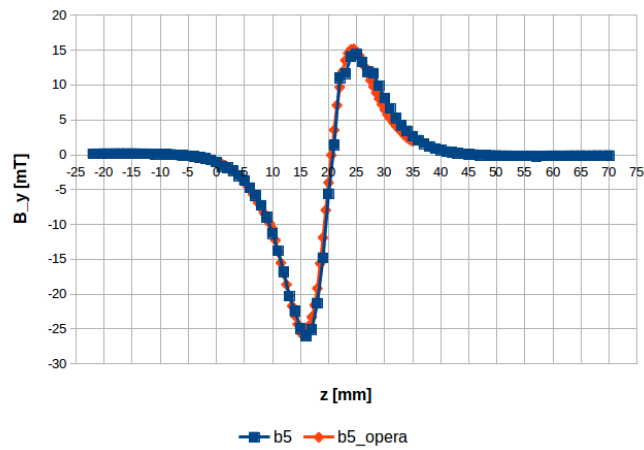

Figure 2.10: Plot of measurements (blue) and Opera simulations (orange) for beamlet 5.
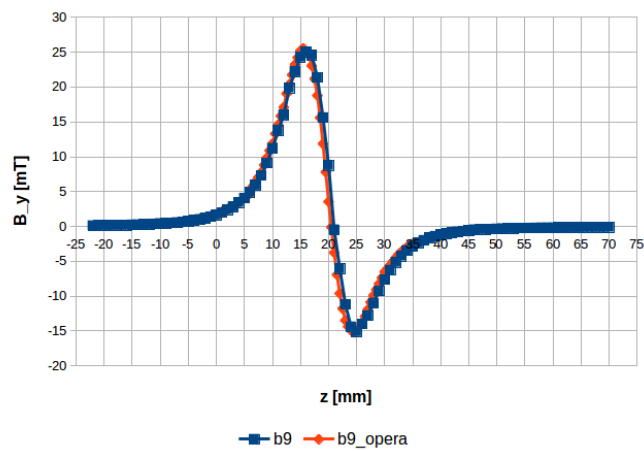

Figure 2.11: Plot of measurements (blue) and Opera simulations (orange) for beamlet 9.

3 Simulations

Numerical simulation is a standard way of designing ion optical devices in the field of ion source and accelerator physics. In the case of ions from a plasma, the plasma boundary where ions are extracted has to be taken into account. So far the plasma modelling of the code has been restricted to positive ion extraction systems. For the case of negative ion plasma extraction few codes exist, most of them capable of 2D modelling only, where simulations are in agreement with experiments. 3D modelling is needed because of the presence of magnets required to deflect co-extracted electrons. The aim of this chapter is to expose the steps done in order to write a C++ based code which simulates the ion beam with the new extraction grid system using the IBSIMU simulation package.

3.1 IBSIMU

IBSIMU [22] is an ion optical computer simulation package used as a computer library through a C++ interface. IBSIMU is able to support definition of electrode geometry and calculation of electric field in 1D, 2D, 3D and cylindrical symmetry (axisymmetric), to calculate particle trajectory in electric and magnetic fields and to simulate positive and negative ion extraction from a plasma. The definition of the geometry of solids can be done using mathematical description or by importing data in standard CAD formats.

The simulation domain is discretized with a regular mesh with constant step size and electrostatic potential is calculated by solving Poisson's equation using FDM finite difference method (where differential equations are solved by approximating them with difference equations) on the nodes of this mesh. On the edges of the simulation domain both Dirichlet and Neumann boundary conditions are supported.

Particle tracer works by integrating the equations of motion with automatic step-size adjustment for required trajectory accuracy by using a Runge-Kutta method from the GNU Scientific Library. This algorithm finds all the mesh squares the trajectory passes through and deposits the charge of the particle on the eight (four, in 2D simulations) surrounding mesh nodes. The electric field used in trajectory calculation is obtained by differentiation and interpolation of potential using 27 closest neighboring mesh nodes.

A typical simulation sequence starts with solving Poisson's equation with a zero charge density (i.e. Laplace equation) as an initial guess and then calculating particle trajectories and space charge density. The space charge is therefore used in Poisson's equation to solve a new potential map. This sequence is repeated until the solution converges to required precision.

3.1.1 Plasma model for negative ion extraction

The negative ion plasma extraction implementation in IBSIMU is based on the existence of an equipotential surface between the bulk plasma and the extraction, where the potential is zero [23] (plasma meniscus). The bulk plasma is assumed to have a positive plasma potential U_p and the extractable ions are assumed to be born close to the wall potential and extracted from a uniform plasma [24].

This potential structure causes positive ions from the bulk plasma to be accelerated towards the extraction and to be reflected back into the plasma by the increasing potential in the extraction, acting as a trap for thermal positive ions. The negative ions and electrons are accelerated from the wall potential towards the bulk plasma and the extraction (see figure 3.1).
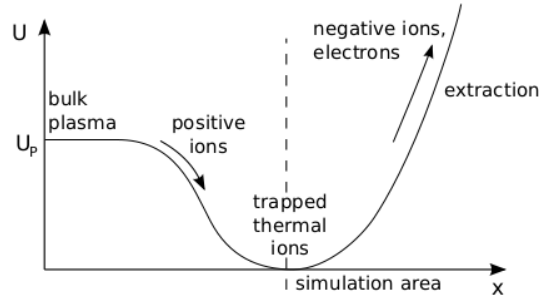

Figure 3.1: Negative ion plasma extraction model from [23].

The simulated area starts from the plasma electrode potential, where the extracted negative ion and electron beams originate from. The negative particle beams are defined by setting current density, initial drift energy and temperature values and integration of the Lorentz force takes into account the electric and magnetic fields (electric field for the first iteration round of the simulation is computed by setting zero space charge density, as discussed in 3.1, and forcing zero potential value inside the estimated plasma volume).

The Poisson equation describing the system in the simulation area is

$$\Delta^2 U = -\frac{\rho}{\epsilon_0} \tag{3.1}$$

where the space charge density ρ is given by $\rho = \rho_{neg} + \rho_f + \rho_{th}$. Here ρ_{neg} is the space charge density of negative particles from ray tracing, ρ_f is the space charge of fast positive ions and ρ_{th} is the space charge of trapped positive thermal ions. Quasi-neutrality of plasma requires $\rho_{neg} + \rho_f + \rho_{th} = 0$ at $U = 0V$, which is typically the boundary of the computational domain. Each of the thermal ion species has a separate Maxwellian velocity with the associated space charge distribution. Space charge distribution ρ_f and ρ_{th} are given by a model which uses values of amount of particles and energy (thermal or directed) given by the user [24].

Negative ion extraction with a dipole magnetic field shows ray-traced particles deflecting already inside the plasma. This happens because particle collisions and cross field diffusion are not being modelled by the simulation [23] (see 2.1.1). The physical fact by which ions and electrons are highly collisional and move diffusively until they are accelerated by the extraction electric field is achieved in the simulation by suppressing the magnetic field at potentials less than a threshold value given by the user. This threshold defines a boundary between the plasma volume where ions and electrons are collisional (electrons are highly collisional until they reach a velocity large enough) and the extraction volume where collisions no longer occur. This threshold value is hard to estimate and, in most cases, is around $1 - 20V$ as it corresponds to the energy range where collisional properties become negligible. Usually ion optics is not very sensitive to this parameter.

3.2 Implementation of a code for NIO beam acceleration

The IBsimu package was largely used in recent years in the context of high energy physics [25] [23] [26] [27]. In this section a description of how the libraries of IBsimu, described in the previous chapter, and routines specifically developed have been used to build up a versatile C++ code that has also been used to model the H- extraction in the case of NIO accelerator. An iterative approach in solving dynamics of beams is used and the basic elements of the final structure of the code written are represented in the following flow chart. Numbers refers to the numbered list.
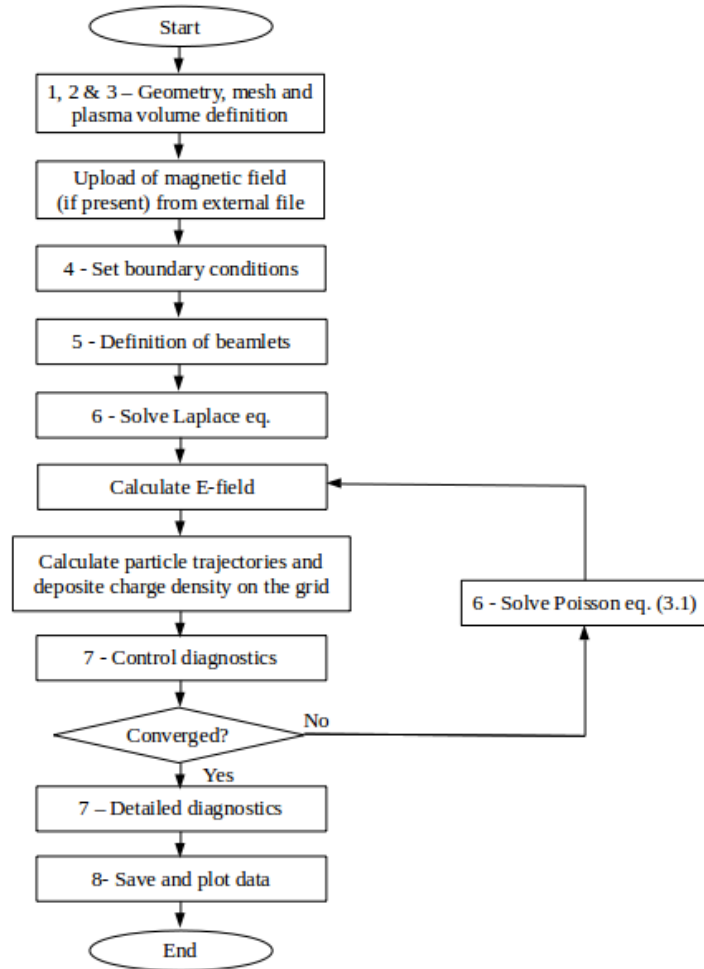
Figure 3.2: General flow chart of the simulations.

1. Definition of geometry by choosing between 3D and axisymmetric; setting (x,y,z)-dimensions of the simulation volume and the mesh unit cell length.

2. Electrode geometry is defined via boolean operation, or by uploading from a CAD file. This is particularly useful for the multi-beamlet simulation, where a mathematical description of the geometry might be difficult.

3. Definition of negative or positive plasma model (setting the plasma volume and an initial guess for plasma meniscus).

4. Set (Dirichlet or Neumann) boundary conditions of electric potential at mesh and grid boundaries.

5. Definition of cylindrical beamlets by setting the number of particles, the current density, charge and mass of a single particle and position, radius and axis of the basis of the initial cylinder where the particles are generated.

6. Poisson equation is solved using BiCGSTAB (biconjugate gradient stabilized method) solver class.

7. Diagnostic tools have been written in order to calculate quantities such as divergence or average angles of the beamlets (a more accurate description of diagnostics performed is deferred to the end of this section). These diagnostics are performed both in the last iteration and in the intermediate iterations in order to keep under control convergence of these parameters.

8. Definition of geometry plotter and saving data for further analysis.

A list of input parameters set by user is shown in table 3.1.

Symbol	Description
N_{it}	Number of iterations
N_i and N_e	Number of simulated ions and electrons trajectories
j_i and j_e	Ion and electron current density
E_b	Initial beam mean energy
r_b	Cylinder base radius for beam definition
U_p	Plasma potential
R_f	Ratio of fast compensating positive ions to total negative charges (3.1.1)
h	Unit cell size
-	Dimensions of mesh volume and initial guess for plasma volume
$V_{PG}, V_{EG}, V_{AG}, V_{REP}$	Potential of grids
U_{sup}	Magnetic field is suppressed at potentials less than U_{sup} (3.1.1)

Table 3.1: Input parameters.

The diagnostics written aim to calculate divergence and average angles of the beamlets. This calculations differ from axysimmetric to 3D geometry and presence of electrons rather than only ions has to be taken into account.

Data of particle positions, velocities and currents for each beamlet (if more than one beamlet is present) are stored for further analysis or immediately processed in order to calculate average angle θ and divergence δ as follows.

For a cylindrically-symmetric beam with no magnetic field divergence δ can be defined as in equation 3.2.

$$\delta = \sqrt{\sum_i \theta_i^2 \left(\frac{I_i}{\sum_j I_j} \right)} \tag{3.2}$$

with

$$\theta_i = \arctan \left(\frac{v_{ri}}{v_{zi}} \right) \tag{3.3}$$

where I_i, v_z and v_r are the current carried by the i-th particle, the axial velocity and transverse velocity of the i-th particle in the cylindrical coordinates.

Another useful quantity in studying beam optics is the average beam angle θ computed as the average of θ_i from equation 3.3 and usually is around 0 in simulations without magnetic field.

In 3D geometries with magnetic field divergence is calculated along x or y axis as in equation 3.4, since magnetic field breaks cylindrical symmetry and δ_x may differ from δ_y. Since, in this case, the average beam angle is not 0 we need to take into account a correction for each θ_i and consider θ_i' as in equation 3.5.

$$\delta_\xi = \sqrt{\sum_i \theta_{\xi i}'^2 \left(\frac{I_i}{\sum_j I_j} \right)} \tag{3.4}$$

with

$$\theta_{\xi i}' = \arctan\left(\frac{v_{\xi i}}{v_{zi}} \right) - \theta \tag{3.5}$$

where ξ can be either x or y.

3.2.1 Sensitivity study of numerical parameters

As a first step, numerical parameters of simulations have been studied in order to choose the best ones from the point of view of results stability at a reasonable simulation time. The term "numerical parameters" refers to all the parameters such as mesh size h, number of particles N and number of cycles performed that do not reflect a variation in the physics equation describing the problem, but only represent the accuracy to be sought after in the solution. Therefore (since numerical parameters are not expected to affect the results of simulations, if a reasonable accuracy is assured for all parameters) the aim of this sensitivity study is to find the optimal values of parameters that make the simulation results stable, without impacting too much on the simulation work load.

Since simulations using 2D axisymmetric geometries take less simulation time (up to 40%) with respect to 3D geometries, the majority of them for numerical and physical parameters study has been done with axisymmetric geometries. In this case only a half of the xy plane is simulated (see figure 3.3) and the axially symmetric version of the Poisson and motion equations are used. Also, a reflection of the particles crossing the symmetry axis ($z = 0$) is imposed.
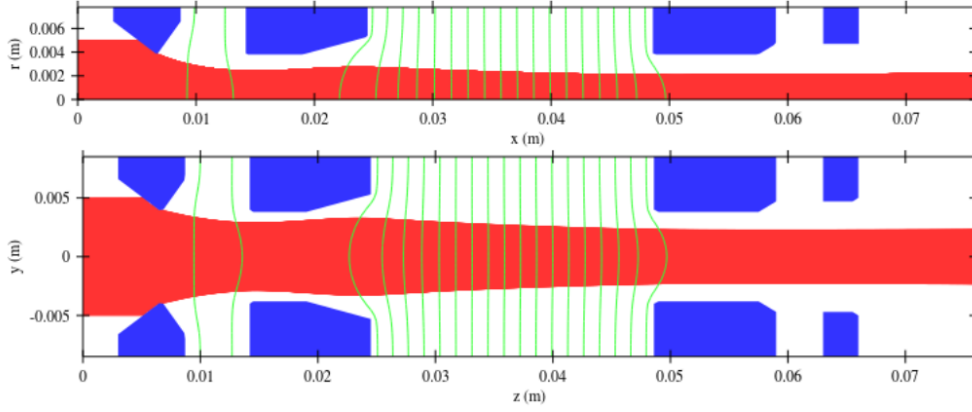
Figure 3.3: Comparison between axisymmetric (top) and 3D (bottom) geometry simulations in absence of magnetic field.

Unless otherwise specified, the other parameters among those listed in table 3.1 have been set to the values shown in table 3.2. These are design target parameters of NIO as calculated in [18].

Parameter	Value
Beam current density	$300A/m^2$
EG potential	$5800V$
AG potential	$57600V$

Table 3.2: Nominal parameters.

Some of the most significant analyses resulting from simulations are shown in the following plots. Since numerical parameters are here studied, they are not expected to affect beam optics under a certain threshold value. Divergence has been chosen as a control parameter for the beam optics and it is represented in figure 3.4 for different values of the unit cell size h. These figures also show the time required for the CPU to complete the simulation on the right y-axis. These simulations, which aim to find the optimal numerical parameters, do not take into account magnetic fields and electrons even in 3D geometries. Hence divergence was calculated using equation 3.2 both in 3D and axysimmetric simulations. In both cases the value of divergence converges for small values of h as expected while the simulation time increases almost exponentially. On this basis, a value of h between $0.1 \div 0.15mm$ was chosen for axysimmetric geometries and between $0.25 \div 0.35mm$ for 3D geometries.

Figure 3.5 represent divergence versus different values of the number of cycles and number of particles N. The value of divergence rapidly converges with number of cycles and keeps its value steadily. A range of $15 \div 25$ iterations has been chosen. Time for simulating one single iteration is about constant for any iteration. Finally, a stable value of divergence is found for a number of particles between $1500 \div 3000$ per beamlet.
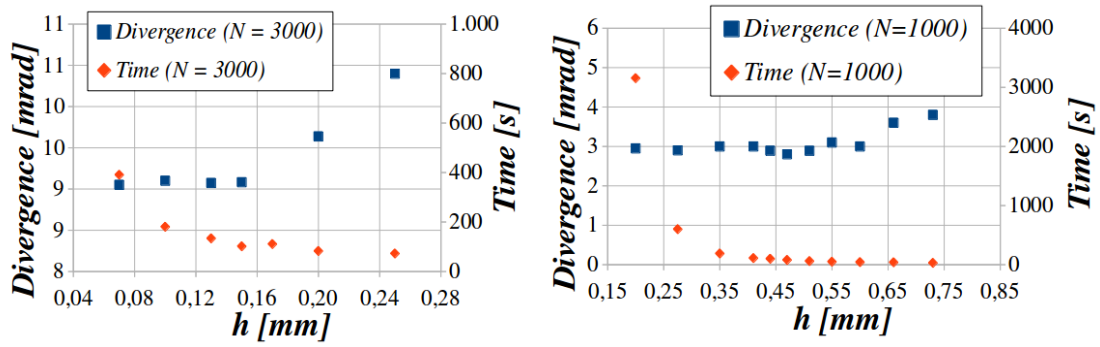
Figure 3.4: Divergence and time of simulation vs h value of the mesh. Axisymmetric simulations on the left and 3D simulations on the right.
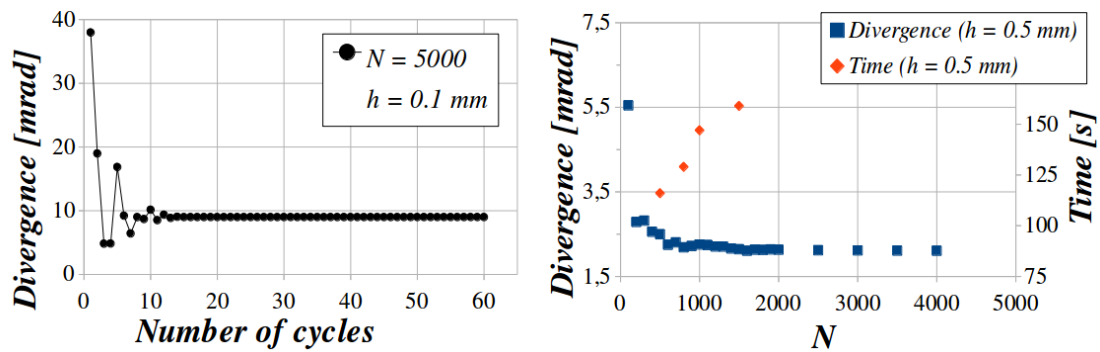

Figure 3.5: Left: Divergence and time of simulation vs number of cycles for axisymmetric simulations; 3D simulations show similar results.
Right: Divergence and time of simulation vs number of particles for 3D simulations; axisymmetric simulations show similar results.

3.2.2 Study of physical parameters

Some parameters set by the user, like plasma potential U_p and R_f value (section 3.2), are used by the code to tune the equation that regulates the extraction of particles in the plasma model and they have to be chosen properly in order to have a stable simulation. The choice of these parameters as well as the choice for the beam energy is based on the results of simulations represented in figure 3.6. These figures refers to axysimmetric simulations with no magnetic field and no electrons but same results have been obtained with 3D geometries with magnetic field and electrons too. Final values chosen are $U_p = 6eV$ and an initial beam mean energy E_b of $8eV$. Divergence stays almost constant for a variation of these parameters but some deviations are displayed for low values of them, which are interpreted as corresponding to unstable situations.

The scan of divergence vs R_f displays a constant behavior for values $R_f = 0 \div 0.3$. For higher values of R_f, corresponding to a plasma model where fast compensating positive ion density is almost the same as the total negative charge, simulations becomes unstable as shown in figure 3.7. Final value chosen is $R_f = 0.2$.
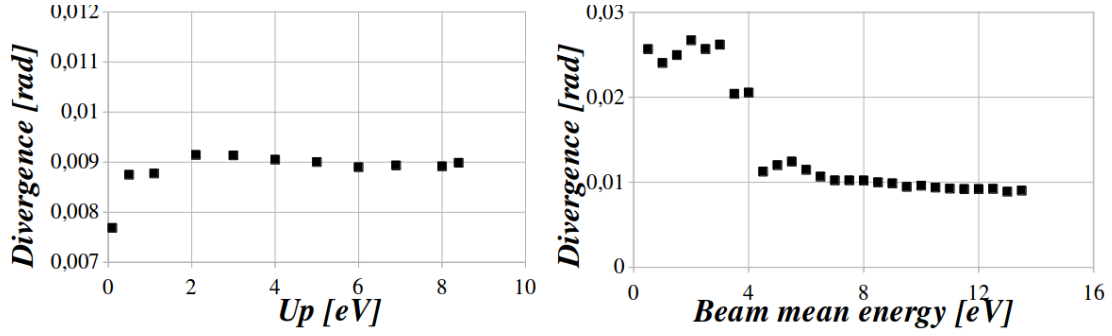
Figure 3.6: Divergence vs plasma potential U_p (left) and initial beam mean energy E_b (right) for axisymmetric simulations (with $N = 1000$, 25 iterations, $h = 0.1 mm$). 3D simulations show similar results.
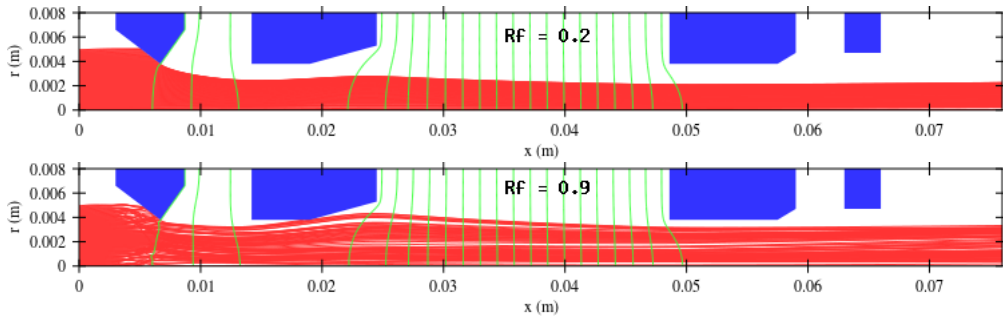

Figure 3.7: Comparison between simulations with different values of R_f.

Parameters chosen in this section and in the previous one are from now on kept fixed. The other parameter listed in 3.1 together with geometry and magnetic field are adjusted depending on the case which is being simulated.

3.3 Code validation

After the choice of the optimal parameters in time and stability, a code validation has been performed as the checking of a simple scaling law discussed in 1.3.2 based on the perveance parameter. As explained, if the beam current density is scaled by a factor η, the divergence is expected to have the same value when voltage is scaled by a factor $\eta^{\frac{2}{3}}$. The two values of beam current density j used for these simulations are $j = 30 \frac{A}{m^2}$ and $j = 300 \frac{A}{m^2}$ corresponding to a scaling $\eta = 0.1$ of the design value of the extracted current. Consequently, the voltages must be rescaled by a factor ≈ 0.215 to maintain the same perveance. All the other parameters are kept fixed. The comparison is done by the values of divergence along z-axis and the results are in a good agreement especially from the repeller position on, as shown in figure 3.8 confirming the expected current scaling with constant perveance.
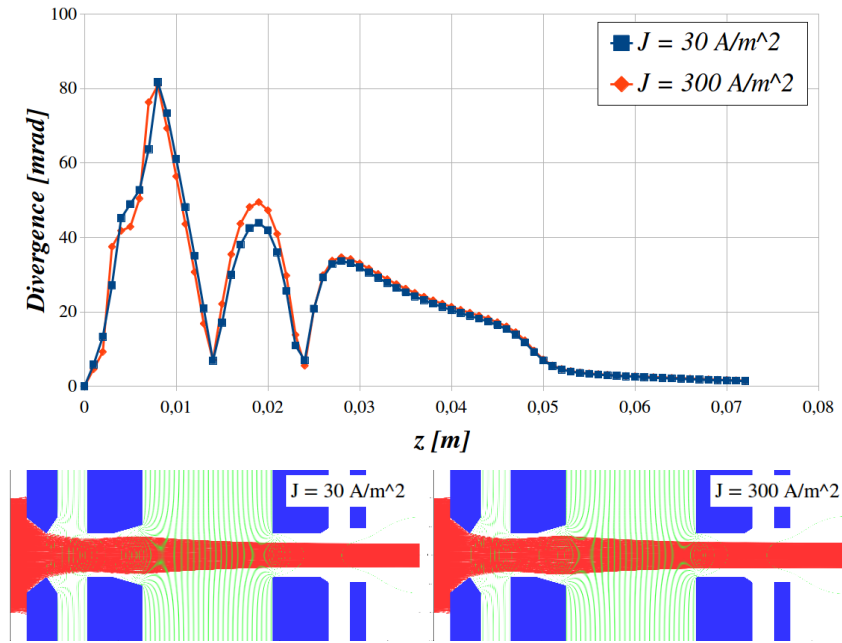
Figure 3.8: Checking the scaling law for $j = 30\frac{A}{m^2}$ and $j = 300\frac{A}{m^2}$. The graph shows divergence vs position on z-axis.

A further test which has been done is comparing the code with the SLACCAD code [28]. The comparison was made by applying the model based on IBSimu to simulate the same scenario scan reported in [18], i.e. a scan over the extraction voltage of the NIO accelerator, performed with SLACCAD.

The results of both simulations are reported in figure 3.9 and the two codes obtain very similar behaviors of divergences and their difference becomes smaller when approaching the minimum region. They show about the same values of divergence calculated at the accelerator exit (10mm after the last electrode) and both display a minimum between 5kV and 5.25kV for the EG voltage. These simulations have been done with no magnetic field since SLACCAD is not able to deal with it.
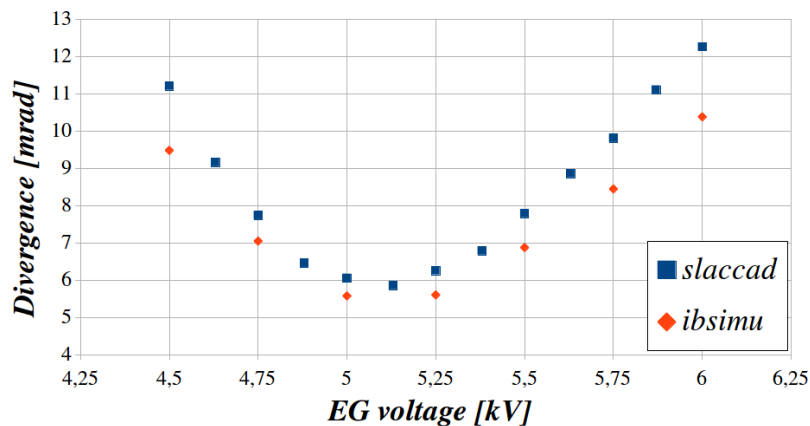

Figure 3.9: Comparison between IBSimu and Slaccad for an EG voltage scan.

4 Study of the new extraction system

The aim of this chapter is a comparison between the current extraction grid configuration described in chapter 2 and the previous one which was carried out by adjusting the code described in the previous chapter.

4.1 Simulations with magnetic field

Since magnetic field and electrons have to be taken into account in order to describe real accelerators, the upload of magnetic field from an external data file and the resulting correction of diagnostics as described in section 3.2 has been performed.

As expected, the insertion of a magnetic field results in the presence of an average angle of deviation of the beam. Figure 4.1 shows the dependence of the average angle on position along z-axis for simulations performed with and without magnetic field on the left and a comparison between B_y trend for the new and old EG magnetic configuration. The first and second peak are due to EG and AG respectively. This angle is about zero along the whole axis without magnetic field but there are deviations in correspondence to the EG and AG positions in the case of simulations with magnetic field. As explained, the EG grid configuration with only CESM magnets has a stronger B_y value which shows a bigger average beam deviation in the region of the EG grid. The simulation shown in this section have been done using nominal parameters.
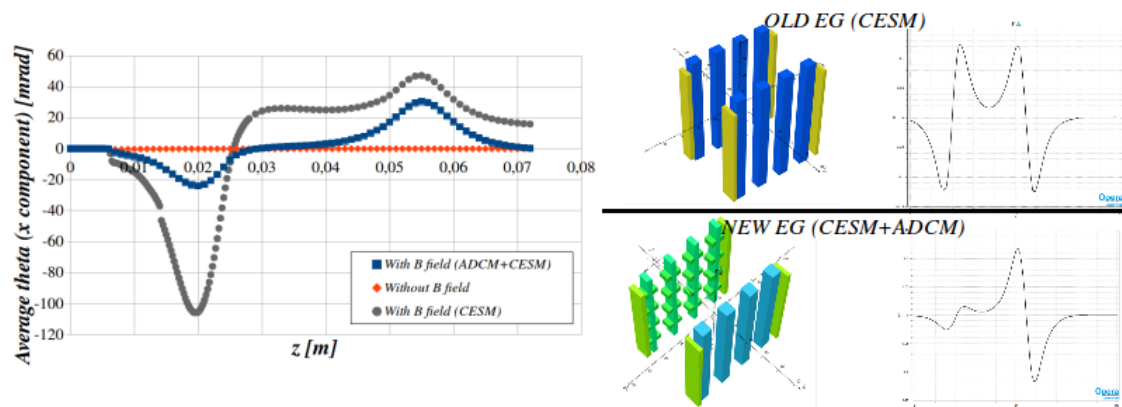

Figure 4.1: Left: average component x of the angle of deviation vs z-axis position for simulations performed with and without magnetic field. Right: comparison between the trends of B_y along z direction (the first peak corresponds to EG, the second one to AG).

4.2 Comparison between the new and old extraction system

Simulations with nominal parameters can clearly reproduce the differences between the beam properties when using CESM or ADCM+CESM magnetic field. As explained in chapter 2, they differ mainly in the value of B_y around EG region, higher for CESM configuration, and ADCM+CESM better satisfies relation 2.1. This implies a stronger deflection of electrons and ions at the exit of the plasma grid as in figure 4.2 (simulation with design parameters but $V_{EG} = 5800V$) or figure 4.1 for the average angle.
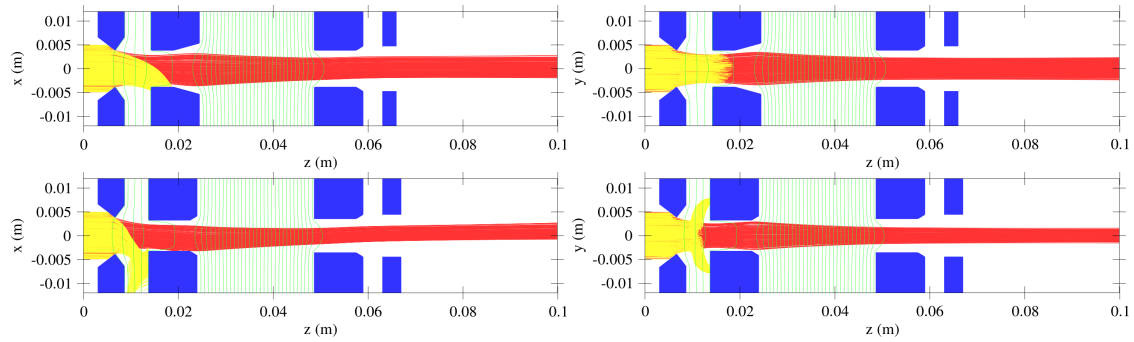

Figure 4.2: Plots of results of simulations with new EG (top) and old EG (bottom).
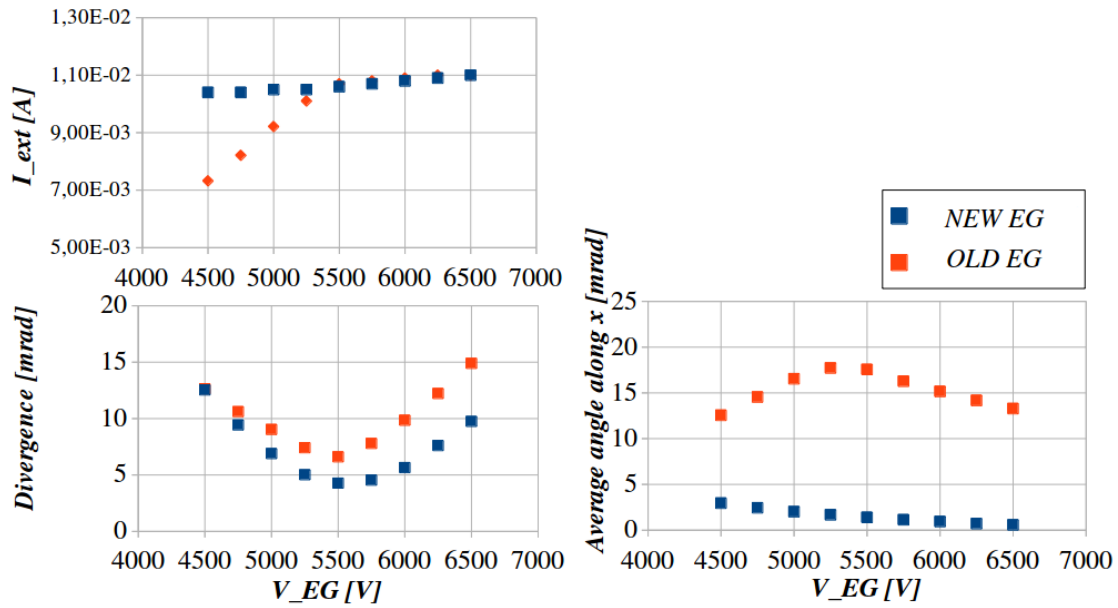

Figure 4.3: Comparison between divergence δ, average angle along x direction θ_x and extracted current in the case of new and old EG configurations.

Results show (figure 4.3) that the minimum value of divergence is reached at about $V_{EG} = 5500V$ for both configurations and new electrode produces a smaller value of divergence, as expected. Extracted current from the REP reaches almost its maximum in the simulations with V_{EG} between $4500 \div 5500V$ for the new electrode. In the old configuration only a smaller extracted current is noticed in that interval since ions hit

27

EG grid in the x-axis direction as can be seen in figure 4.2. The average angle along x-axis is smaller in simulations with the new electrode configuration for any value of V_{EG}. The average angle along y-axis is about zero in both cases as explained in section 2.1.

The study of velocity components can be useful to discuss the beam deflection. As shown in figure 4.4, v_x spectra is between 20 and $60 km/s$ in the case of the old electrode and zero centered in the case of the new EG. It means that the beam, in the old electrode, will deflect in x direction more than it does in the new EG configuration.
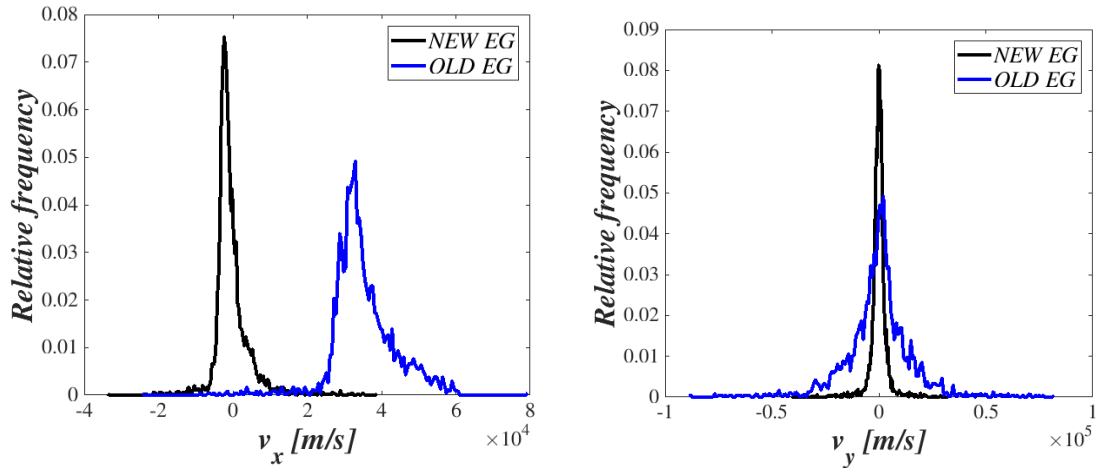
Figure 4.4: Histogram of relative frequencies of v_x and v_y at the exit of REP.

Finally, although the beamlet divergences are similar for the 2 grids, the new grid works better because it has a much lower deflection at all the EG values tested, and because it extracts and accelerates more beam current than the old configuration for which, for low EG values, a part of the beam is intercepted by the extraction grid and a fraction of the current is lost (up to 30% less).

5 Simulations with experimental parameters

The code written and tested can reproduce the main differences between the two EG configurations. This chapter will focus on the new EG configuration (featuring CESM+ADCM magnets) with the aim to reproduce and explain experimental data.

With this purpose, the first implementation performed on the IBSimu code has been to modify the geometry, boundary conditions and number of particle emitters (approximating the extraction from a plasma) in order to simulate the full domain of the NIO1 accelerator, including all the 9 beamlets. This allows to take into account also the effect of mutual repulsion among neighbouring beamlets. Geometry has been created and loaded from a CAD file.

5.1 Beam emission spectroscopy

Since experimental data are used in this chapter, a basic exposition of how beam divergence and spectra are measured in NIO1 is required. A set of diagnostics monitors the operation of NIO. Some of them are CCD cameras and beam emission spectroscopy (BES). In particular, the two CCD cameras, like the one represented in figure 5.1, can measure the total emission of visible line along the x and y axis of the accelerator.

Beam emission spectroscopy measures the uniformity and the divergence of the fast particle beam exiting the ion source and traveling through the beam line components. This type of measurement is based on the collection of the H_α emission resulting from the interaction of the energetic particles with the background gas [29]. The divergence δ of the beamlets can be measured from the spectral width of the shifted H_α component (see figure 5.1). This line, indeed, is broadened by the Doppler effect by a quantity which depends on the beam divergence δ.
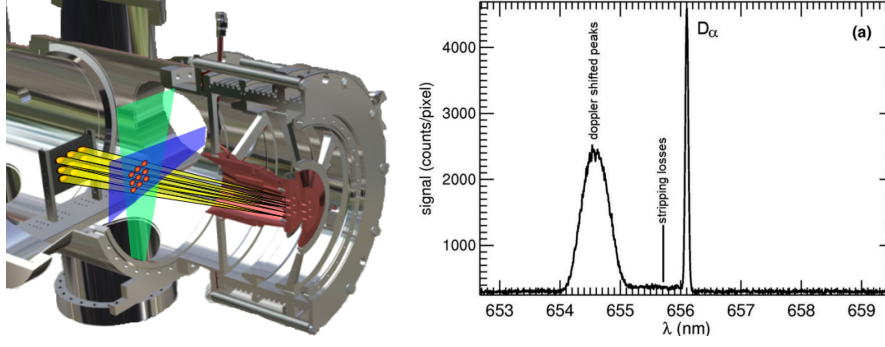
Figure 5.1: Left: CCD cameras with the 9 beams. Right: typical spectra obtained by the simulations for a horizontal lines of sight [29].

The experimental data shown in this chapter were taken with V_{EG} and V_{AG} values much smaller than the design target parameters of NIO reported in table 3.2. This is due to the fact that NIO source is actually working in pure volume operation, i.e. in the absence of cesium vapors, that will be used to enhance the negative ion production (as explained in section 1.3.1) in a second stage. Therefore the extractable ion current is much less (and the electron current is much higher) than the design values. This consequently limits the values of voltages, (perveance scaling). The following table 5.1 shows the experimental working parameters used in this chapter.

Parameter	Value
Electron current density j_e	$250 A/m^2$
Ion current density j_i	$1.5 A/m^2$
EG potential V_{EG}	$300 V$
AG potential V_{AG}	$1000 \div 5000 V$

Table 5.1: Experimental working parameters.

5.2 Comparison between simulations and experimental data

Simulations have been performed with different values of AG potential, whose range is reported in table 5.1. A particle trajectory plot relative to the cases with $V_{AG} = 1000V$, $3000V$ and $5000V$ is shown in figure 5.2. These plots represent the 9 beams superimposed as they appear if looked from x or y direction. Therefore, the opposite deflection of beam in different columns (see section 2.3) can be observed, especially in $V_{AG} = 5000V$.
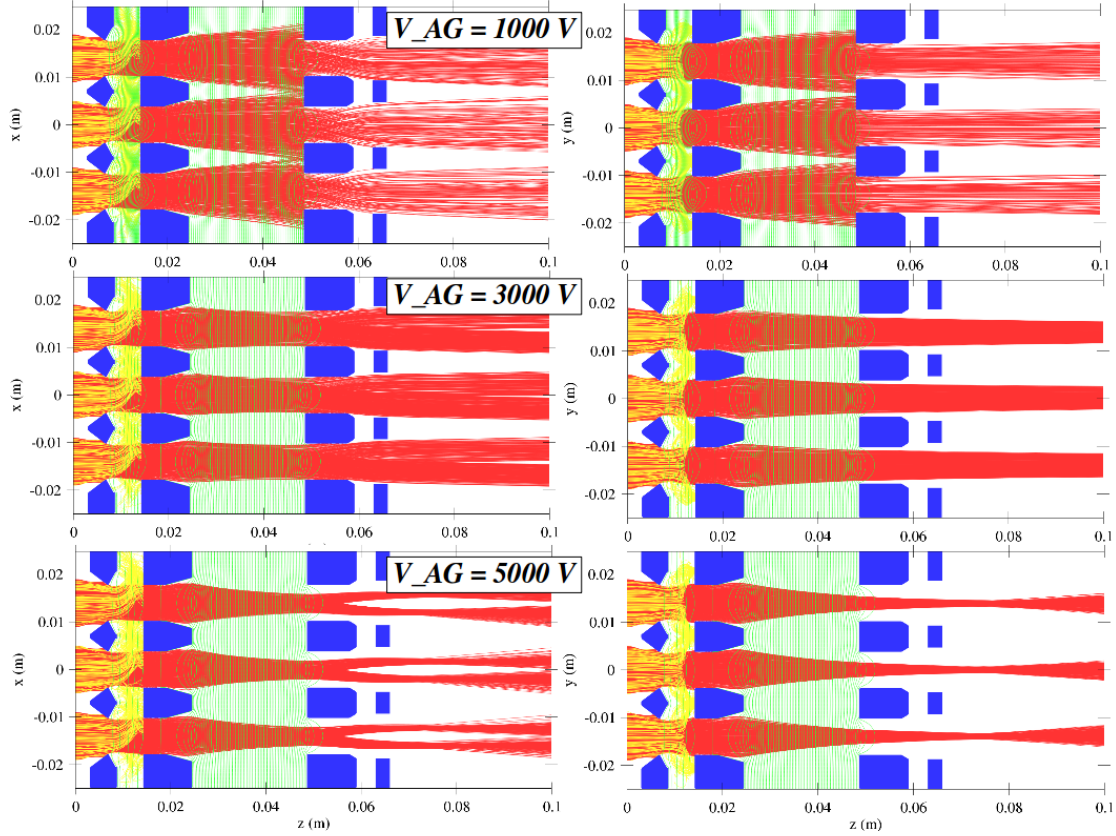
Figure 5.2: Plots of ZX (left) and ZY (right) graphs from simulations for three values of V_{AG}.

The results of simulations have been compared to the experimental data by computing divergence and extracted current from the REP. The beam spectra at the CCD camera position (figure 5.1) resulting from the simulations have been compared to the experimental one obtained from the CCD cameras.

The values of divergence represented in figure 5.3 are obtained from simulations and experimentally from the beam emission spectroscopy. They show the same trend and both have the minimum for about $V_{AG} = 2750V$.
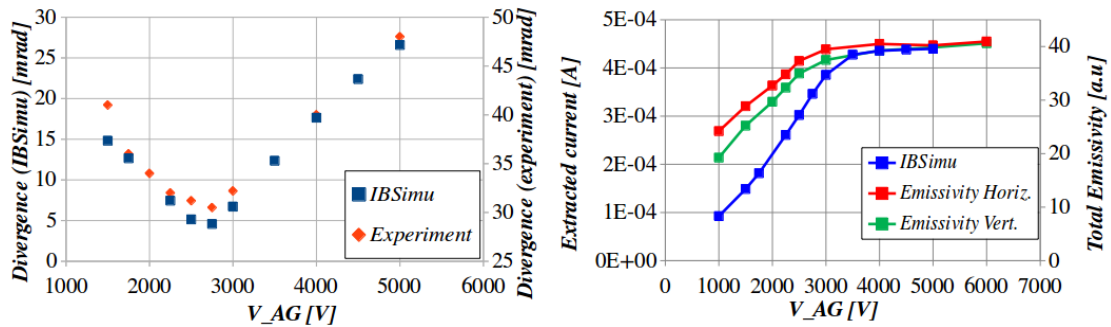

Figure 5.3: Divergence (left) and extracted current (right) scan in V_{AG}.

The accelerated current is the current carried by the beam exiting the REP in the case of simulations and computed as the integral of CCD signal in the case of experimental values. Its scan in V_{AG} is reported in figure 5.3 where an agreement in the trend of experimental and numerical results can be appreciated. The main difference that can be seen is in the value where the maximum extractable current is reached. Experimentally, both in the vertical (x) and horizontal (y) direction, the accelerated current reaches its maximum in the range $V_{AG} = 2500 \div 3000V$. This value is reached at higher values of AG voltage, between $3500 \div 4000V$ if the trend obtained from simulations is considered.

The profiles of beam current can be deduced from the numerical simulation and projected onto the diagnostic plane xy where the CCD cameras are installed, in order to compare directly the beam profiles. The comparison is reported in figure 5.5. Figure 5.4 shows the origin of the 3 peaks in y direction and 4 peaks in x direction at V_{AG}. When the beam optics is good (low divergence) the beamlets are well distinguishable, whereas they tend to overlap in a single and wider peak when the optics is worse (and the divergence increases). As can be deducible from figures 5.2 and 5.3, the good optics is found for intermediate AG values (around VAG=3000 V). The area under these profiles is the extracted current values reported in figure 5.3. The difference in the value of AG voltage in which the extractable current reaches its maximum in the of simulations and experiment explains why profiles obtained at $V_{AG} = 3000 \div 4000V$ converge to the one with $V_{AG} = 5000V$ faster in the experimental than the simulation case. Finally, it is worth noticing that signal from the experiment have a diffused background of about 20% of the overall signal due to the formation of an emissive plasma during interaction of the beam with the neutral gas present in the drift region. This background tends to hide the emission purely induced in the beam area.
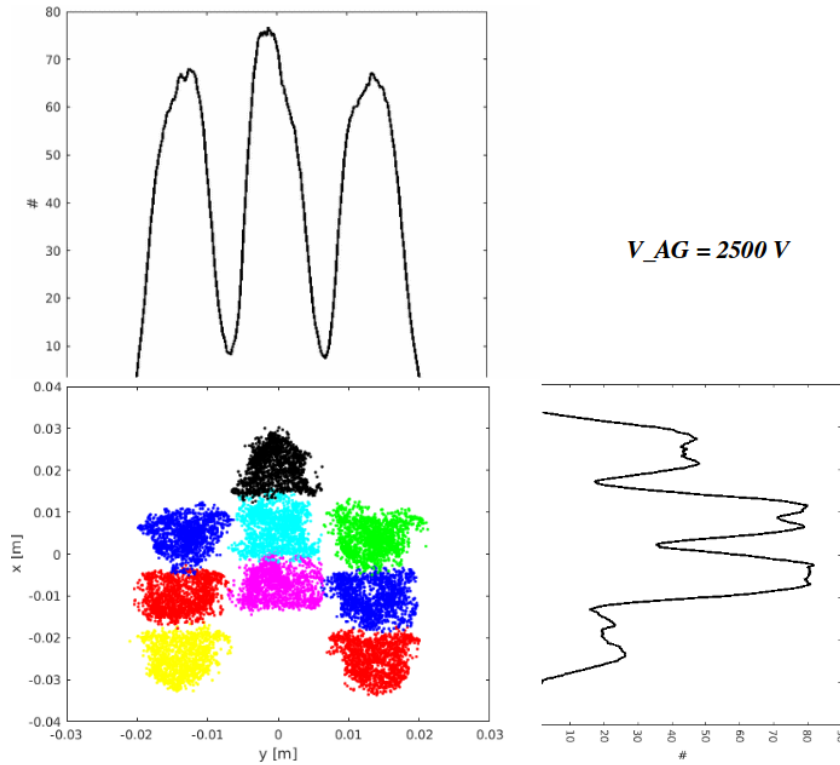
Figure 5.4: Simulated beamlet footprints at the diagnostic plane (400mm from the REP exit) and transversal profiles of the beam (in a.u.) with $V_{AG} = 2500V$.
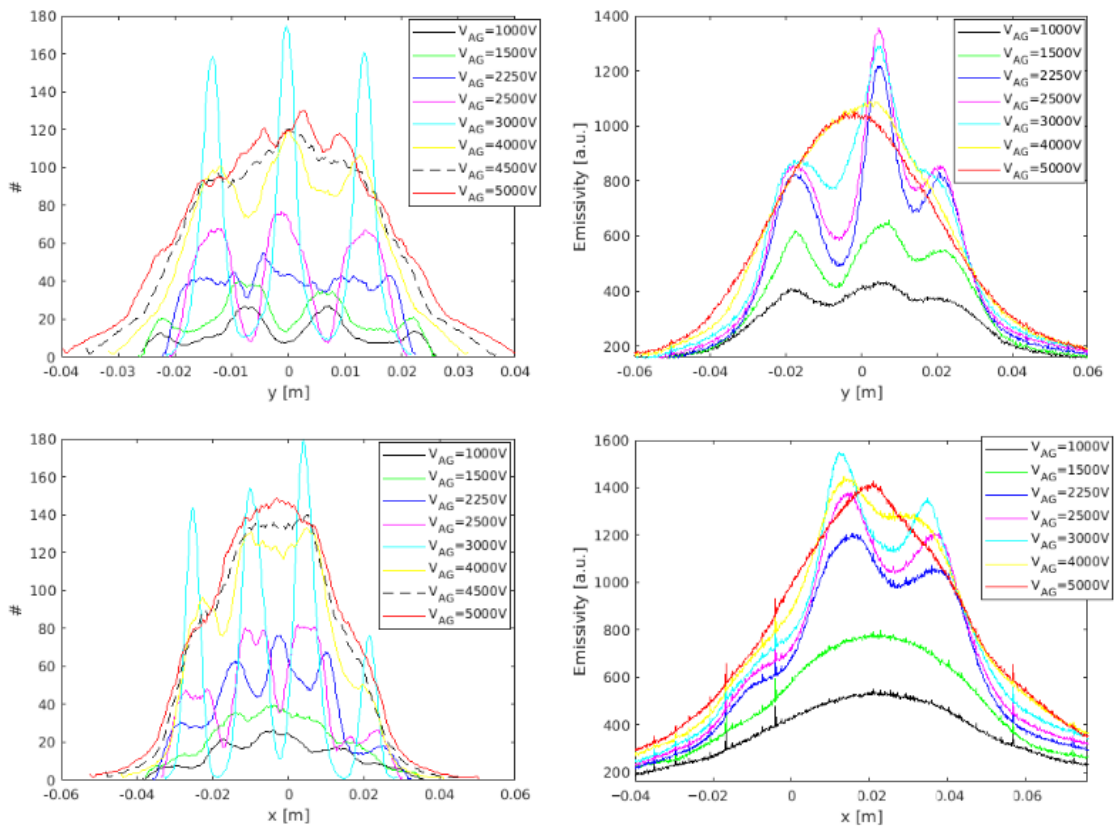

Figure 5.5: Spectra from simulations (left) and experimental data (right).

6 Conclusions

This thesis presents a preliminary study of neutral beam injectors and the theoretical and numerical researches supporting the new geometry and magnets for the NIO extraction grid was performed. The magnet measurement and grid installation to NIO were also carried out. The activity focuses on the writing and testing of a numerical code for simulating the acceleration of a negative beam from a cold plasma based on IBSimu libraries. This code has shown to be better in versatility and required less CPU time for a simulation with respect to other codes previously used for studying NIO in Consorzio RFX. A comparison of this new code with the other modeling tools previously used showed a good agreement in their results, evaluated in terms of the beam divergence in a number of different conditions.

The code has then been used to compare the current extraction grid configuration and the previous one. It has been shown that the extracted ion beam from the new EG is better in terms of divergence, average deflection and extractable current of the beam as displayed in figure 4.3. Moreover its magnets can divert electrons with the least impact on the ion beam deflection.

Finally, a comparison of the code with experimental data from the first operations of NIO with the new EG has been performed. A good overall agreement has been found between experiment and simulations with some differences mainly due to physical phenomena which are still not included in the simulations. Differences in experimental and simulated profiles in figure 5.5 could be explained considering the interaction between beam and background gas. Ions H^-, in fact, can loose one electron when colliding with the residual ion gas present in the accelerator. These fast neutrals formed in the accelerator only feel a portion of the optimized electric field profiles, and then proceed ballistically toward the accelerator exit. The presence in the beam of such particles, having a much higher divergence than the bulk H- beam component will affect the beam profiles measured by CCD and BES.

Therefore, as a future improvement of the code, the inclusion of collision phenomena of the beam with the gas is envisaged. This can be addressed with probabilistic (Monte Carlo) methods, and the secondary particles produced included in the beam model. This could improve the reliability of numerical simulations.

Bibliography

[1] M. Kikuchi, K. Lackner, and M. Q. Tran, "Fusion Physics", *International atomic energy agency*, 2012.

[2] S. Atzeni and J. Meyer-ter-Vehn, "The Physics of Inertial Fusion", *Oxford University Press*, 2009.

[3] ITER official site, www.iter.org.

[4] ENEA official site, www.fusione.enea.it.

[5] J. PAMELA, "The physics of production, acceleration and neutralization of large negative ion", *Plasma Phys. Control. Fusion*, vol. 37, 1995.

[6] M. Bacal, A. M. Bruneteau, C. Deniset, L. I. Elizarov, F. Sube, A. Y. Tontegode, and J. H. Whealton, "Effect of cesium and xenon seeding in negative hydrogen ion sources", *Review of Scientific Instruments*, vol. 71, no. 2, pp. 1082–1085, 2000.

[7] E. Speth, *Nuclear Fusion*, vol. 46, S220, 2006.

[8] Tipler and Llewellyn, "Modern Physics, 3rd Ed.", *Ch 3*, 1999.

[9] M. Bacal and G. W. Hamilton, "H- and d- production in plasmas", *Phys. Rev. Lett.*, vol. 42, pp. 1538–1540, 23 Jun. 1979.

[10] C. D. Child, "Discharge from hot cao", *Phys. Rev. (Series I)*, vol. 32, pp. 492–511, 5 May 1911.

[11] J. R. Coupland, T. S. Green, D. P. Hammond, and A. C. Riviere, "A study of the ion beam intensity and divergence obtained from a single aperture three electrode extraction system", *Review of Scientific Instruments*, vol. 44, no. 9, pp. 1258–1270, 1973.

[12] M. Cavenago, T. Kulevoy, S. Petrenko, V. Antoni, M. Bigi, E. Gazza, M. Recchia, G. Serianni, and P. Veltri, "Design of a versatile multiaperture negative ion source", *Review of Scientific Instruments*, vol. 81, no. 2, 02A713, 2010.

[13] M. Cavenago, T. Kulevoy, S. Petrenko, G. Serianni, V. Antoni, M. Bigi, F. Fellin, M. Recchia, and P. Veltri, "Development of a versatile multiaperture negative ion source", *Review of Scientific Instruments*, vol. 83, no. 2, 02A707, 2012.

[14] M. Cazzador, M. Cavenago, G. Serianni, and P. Veltri, "Semi-analytical modeling of the nio1 source", *AIP Conference Proceedings*, vol. 1655, no. 1, p. 020 014, 2015.

[15] G. Chitarin, P. Agostinetti, D. Aprile, N. Marconato, and P. Veltri, "Cancellation of the ion deflection due to electron-suppression magnetic field in a negative-ion accelerator", *Review of Scientific Instruments*, vol. 85, no. 2, 02B317, 2014.

[16] C. Baltador, M. Cavenago, P. Veltri, and G. Serianni, "Finite elements numerical codes as primary tool to improve beam optics in nio1", *AIP Conference Proceedings*, vol. 1869, no. 1, p. 030 029, 2017.

[17] K. Halbach, "Design of permanent multipole magnets with oriented rare earth cobalt material", *Nuclear Instruments and Methods*, vol. 169, pp. 1–10, February 1980.

[18] P. Veltri, M. Cavenago, and C. Baltador, "Design of the new extraction grid for the nio1 negative ion source", *AIP Conference Proceedings*, vol. 1655, no. 1, p. 050 009, 2015.

[19] M. Cavenago, G. Serianni, M. D. Muri, P. Agostinetti, V. Antoni, C. Baltador, M. Barbisan, L. Baseggio, M. Bigi, V. Cervaro, F. D. Agostini, E. Fagotti, T. Kulevoy, N. Ippolito, B. Laterza, A. Minarello, M. Maniero, R. Pasqualotto, S. Petrenko, M. Poggi, D. Ravarotto, M. Recchia, E. Sartori, M. Sattin, P. Sonato, F. Taccogna, V. Variale, P. Veltri, B. Zaniol, L. Zanotto, and S. Zucchetti, "First experiments with the negative ion source nio1", *Review of Scientific Instruments*, vol. 87, no. 2, 02B320, 2016.

[20] OPERA official site, http://operafea.com/.

[21] F.W.Bell official site, buy.fwbell.com/gaussmeters.

[22] T. Kalvas, O. Tarvainen, T. Ropponen, O. Steczkiewicz, J. Ärje, and H. Clark, "Ibsimu: A three-dimensional simulation software for charged particle optics", *Review of Scientific Instruments*, vol. 81, no. 2, 02B703, 2010.

[23] T. Kalvas, O. Tarvainen, H. Clark, J. Brinkley, and J. Ärje, "Application of 3d code ibsimu for designing an h-/d- extraction system for the texas a&m facility upgrade", *AIP Conference Proceedings*, vol. 1390, no. 1, pp. 439–448, 2011.

[24] T. Kalvas, "Development and use of computational tools for modelling negative hydrogen ion source extraction systems", *Academic Dissertation for the Degree of Doctor of Phylosophy*, University of Jyväskylä, 2013.

[25] T. Kalvas, R. F. Welton, O. Tarvainen, B. X. Han, and M. P. Stockli, "Simulation of h- ion source extraction systems for the spallation neutron source with ion beam simulator", *Review of Scientific Instruments*, vol. 83, no. 2, 02A705, 2012.

[26] C. A. Valerio-Lizarraga, J.-B. Lallement, I. Leon-Monzon, J. Lettry, Ø. Midttun, and R. Scrivens, "Space charge compensation in the linac4 low energy beam transport line with negative hydrogen ions", *Review of Scientific Instruments*, vol. 85, no. 2, 02A505, 2014.

[27] D. A. Fink, J. Lettry, Ø. Midttun, R. Scrivens, D. Steyaert, and C. A. Valerio-Lizarraga, "Optimization of the beam extraction systems for the linac4 h- ion source", *AIP Conference Proceedings*, vol. 1655, no. 1, p. 030 006, 2015.

[28] J. Pamela, "A model for negative ion extraction and comparison of negative ion optics calculations to experimental results", *Review of Scientific Instruments*, vol. 62, no. 5, pp. 1163–1172, 1991.

[29] M. Barbisan, B. Zaniol, and R. Pasqualotto, "Modeling and simulation of a beam emission spectroscopy diagnostic for the iter prototype neutral beam injector", *Review of Scientific Instruments*, vol. 85, no. 11, 11E430, 2014.